Nano Research

ISSN 1998-0124 CN 11-5974/O4
https://doi.org/10.1007/s12274-022-4197-6

Research Article

Ligand centered electrocatalytic efficient CO_2 reduction reaction at low overpotential on single-atom Ni regulated molecular catalyst

Jiazhi Wang[1,2], Qi Hao[1,3], Haixia Zhong[4], Kai Li[1], and Xinbo Zhang[1,2] (✉)

[1] *State Key Laboratory of Rare Earth Resource Utilization, Changchun Institute of Applied Chemistry, Chinese Academy of Sciences, Changchun 130022, China*
[2] *University of Science and Technology of China, Hefei 230026, China*
[3] *Key Laboratory of Automobile Materials, Ministry of Education, Jilin University, Changchun 130022, China*
[4] *Center for Advancing Electronics Dresden (cfaed) and Faculty of Chemistry and Food Chemistry, Technische Universität Dresden, Dresden 01062, Germany*

Received: 9 January 2022 / **Revised:** 24 January 2022 / **Accepted:** 25 January 2022

ABSTRACT

Electrochemical CO_2 reduction reaction (CO_2RR) into value-added chemicals/fuels is crucial for realizing the sustainable carbon cycle while mitigating the energy crisis. However, it is impeded by the relatively high overpotential and low energy efficiency due to the lack of efficient electrocatalysts. Herein, we develop an isolated single-atom Ni catalyst regulated strategy to activate and stabilize the iron phthalocyanine molecule (Ni SA@FePc) toward a highly efficient CO_2RR process at low overpotential. The well-defined and homogenous catalytic centers with unique structures confer Ni SA@FePc with a significantly enhanced CO_2RR performance compared to single-atom Ni catalyst and FePc molecule and afford the atomic understanding on active sites and catalytic mechanism. As expected, Ni SA@FePc exhibits a high selectivity of more significant Faraday efficiency (≥ 95%) over a wide potential range, a high current density of ~ 252 $mA\cdot cm^{-2}$ at low overpotential (390 mV), and excellent long-term stability for CO_2RR to CO. X-ray absorption spectroscopy measurement and theoretical calculation indicate the formation of NiN_4-O_2-FePc heterogeneous structure for Ni SA@FePc. And CO_2RR prefers to occur at the raised N centers of NiN_4-O_2-FePc heterogeneous structure for Ni SA@FePc, which enables facilitated adsorption of *COOH and desorption of CO, and thus accelerated overall reaction kinetics.

KEYWORDS

single-atom Ni, iron phthalocyanine, molecular catalyst, carbon dioxide reduction reaction, ultra-low overpotential

1 Introduction

Electrochemical carbon dioxide reduction reaction (CO_2RR) into value-added chemicals or fuels, associated with renewable energies, is emerging as a prospective route to close the carbon loop while mitigating relevant environmental and energy crisis [1–3]. For example, CO_2RR to CO represents one immediate way to realize the sufficient CO_2 conversion for the faster conversion rate compared to the multiple carbon products and the established industrial utilization of CO for high value-added chemicals and fuels. Unfortunately, the inert nature of the CO_2 molecule and the faster competitive hydrogen evolution reaction (HER) bring grand challenges in driving a stable CO_2RR process with a sufficient current density and high selectivity at low potential [4, 5]. To overcome the above challenges, numerous catalysts have been developed to promote the CO_2RR process [6–8]. However, simultaneously boosting their activity, selectivity, and stability toward high-efficiency CO_2RR remains a grand challenge [9]. Meanwhile, the rational design of an effective electrocatalyst for CO_2RR is hindered by the lack of insightful fundamental study on catalytic site and reaction mechanisms.

To this end, transition metal complex-based molecular catalyst would be one compelling candidate for the high-performance electrocatalytic CO_2RR with respect to its uniform and well-defined active sites, maximum atomic utilization, and tunable catalytic structure [10–12]. Considering the well-defined coordination environment, it also offers an ideal platform to unveil the catalytic reaction mechanism. For example, metal phthalocyanine or porphyrin-based molecules on carbon nanotubes have been widely investigated as the most promising molecular catalysts for CO_2RR [13]. Despite great promise, these molecular catalysts still suffer from low current density, high overpotential, and fast deactivation of catalytic sites. Given that these planar M–N_4 structures of these molecular catalysts can be modulated by the extra coordination with the electron-donating species like O and S groups in axial direction [14], coupling these metal complexes with advanced substrates like functional carbons is expected to be one effective strategy to enhance the activity while stabilizing the active molecules [15]. In this respect, hybrids of the molecular catalyst loaded on a single atom incorporated carbon (M SA/CN) via O linkage are considered as an attractive electrocatalyst for CO_2RR to CO. This is because: I) The atomically and uniform dispersion of a single atom of the M SA/CN substrate can regulate and stabilize the molecular catalytic center toward high-performance electrocatalysis; II) The

---

Address correspondence to xbzhang@ciac.ac.cn

structural advantages of M SA/CN substrate like good conductivity and the porous structure can be beneficial for sufficient mass/electron transport and large current density [16]; III) The preserved well-defined molecular catalytic sites are favored for gaining depth insights into the reaction mechanism [17–21].

In this work, we develop an isolated single-atom Ni catalyst regulated strategy to activate and stabilize the iron phthalocyanine molecule (Ni SA@FePc) as an effective and selective electrocatalyst for a fast CO_2RR process at low overpotential. The resultant Ni SA@FePc shows an excellent electrocatalytic CO_2RR performance regarding its low Tafel slope of 102.7 $mV{\cdot}dec^{-1}$ and large CO partial current density (j_{CO}) of ~ 252 $mA{\cdot}cm^{-2}$ at an ultralow overpotential of 0.39 V and outstanding CO selectivity with Faradaic efficiency (FE_{CO}) above 95% over a potential range from −0.15 to −0.50 V vs. reference hydrogen electrode (RHE), as well as robust stability for 20 h continuous electrolysis. The extended X-ray absorption fine structures (EXAFS) analysis and theoretical calculations verify the formation of NiN_4-O_2-FePc structures for Ni SA@FePc and its contribution to stabilizing the FePc molecule. Density functional theory (DFT) calculations illustrate that such NiN_4-O_2-FePc heterogeneous structure will break the symmetric charge distribution of FePc and enable a distinct reduction of the energy barrier for the adsorption of *COOH, thus resulting in rapid CO_2RR kinetics on the raised N atoms adjacent to the Fe atom rather than Ni and Fe sites. Our work highlights the potential of regulating and stabilizing the molecular catalysts by single-atom materials for a highly effective strategy to boost efficient electrochemical CO_2RR and atomic understanding of the catalytic process.

2 Experimental

2.1 Chemicals

Nickel(II) acetate tetrahydrate (Aladdin, N112914, $NiC_4H_6O_4{\cdot}4H_2O$, 99%), dicyandiamide (Aladdin, D100429, $C_2H_4N_4$, 98%), 2,2'-bipyridine (Aladdin, D108977, $C_{10}H_8N_2$, > 97%), iron(II) phthalocyanine (Aladdin, $C_{32}H_{16}FeN_8$, purified by sublimation, > 98%), potassium bicarbonate (Aladdin, P110485, $KHCO_3$, 99.5%), potassium hydroxide (Aladdin, P301749, KOH, 95%), ethanol (Beijing Chemical Works, C_2H_5OH, B0301002, ≥ 99.8%), N, N-dimethylformamide (DMF, Aladdin, D119450, C_3H_7NO, 99.8%), sulfuric acid (Aldrich, 339741, H_2SO_4, 99.999%), hydrochloric acid (Beijing Chemical Works, A0300003, HCl, 35.0%–38.0%), 5% Nafion solution (Dupont, D520), 212 Nafion membrane (Alfa Aesar), and other chemicals were used directly without purification. The water used was ultrapure water.

2.2 Instrumentation

Powder X-ray diffraction (PXRD) patterns were obtained from an X-ray diffractometer (micro-XRD, Rigaku, Japan) with Cu Kα (λ = 0.15406 nm). Scanning electron microscopy (SEM) images were acquired by a field emission scanning electron microscope (Hitachi S4800) operating at an accelerating voltage of 10 kV. Transmission electron microscopy (TEM) images were carried out on a JEM-2100F instrument with a field emission gun operating at 200 kV. High-angle annular dark-field scanning transmission electron microscopy (HAADF-STEM) images and corresponding energy-dispersive spectroscopy mapping were recorded by an FEI Titan Themis 60–300 instrument with a spherical aberration corrector working at 200 kV. Raman spectra were performed on a micro-Raman spectrometer (Renishaw). Fourier transform infrared (FT-IR) spectra were measured at 298 K on a NEXUS-670 spectrometer. X-ray absorption fine structures (XAFS) were collected on the beamline BL07A1 in NSRRC and were provided technical support by Ceshigo Research Service “www.ceshigo.com”. The radiation was monochromatized by a Si (111) double-crystal monochromator. X-ray absorption near-edge structures and extended X-ray absorption fine structures data were processed by Athena software. N_2 adsorption and desorption isotherms were carried out on a Micromeritics ASAP 2020 adsorption analyzer. X-ray photoelectron spectroscopy (XPS) analysis was carried out on a ThermoFisher Scientific ESCALAB 250Xi instrument. All spectra were calibrated according to the C1s binding energy at 284.4 eV. Electrochemical measurements were performed using a Biologic VMP3 electrochemical workstation at room temperature. ^{1}H nuclear magnetic resonance (NMR) spectra were recorded on Bruker NMR spectrometers (AVANCE-III HD 500). Gas components analysis was performed on ThermoFisher Trace 1300 gas chromatography with pulsed discharge detector (PDD) and flame ionization detector (FID).

2.3 Synthesis of Ni SA/CN

Firstly, nickel(II) acetate tetrahydrate (8.5 mg) and 2,2'-bipyridine (12.1 mg) were dissolved in 2 mL of ethanol, and stirred for 2 h at room temperature to obtain a violet solution. Subsequently, carbon substrate synthesized by pyrolyzing sodium citrate tribasic dihydrate (1 g) was added to the above solution and stirred for 12 h. The resulting black paste was dried in an oven at 70 °C for 12 h and then ground with dicyandiamide (100 mg) in a mortar. The mixture was placed in the porcelain and heated at 800 °C under Ar atmosphere for 2 h. The black product was separately washed with HCl, ultrapure water, and ethanol for several times and dried in an oven at 70 °C for 12 h.

2.4 Synthesis of Ni SA@FePc

Ni SA@FePc was synthesized via a self-assembly method under liquid conditions. Typically, iron(II) phthalocyanine (3 mg) was first dissolved in 60 mL of DMF by stirring for 6 h under the ambient condition to obtain a dark green solution without further color change. Then, the as-prepared Ni SA/CN (30 mg) was added to the above solution, followed by continuously stirring for 12 h. The solid product was acquired by vacuum filtration and then washed with DMF and ethanol for several times until the supernatant became colorless and transparent. The Ni SA@FePc was harvested by drying in an oven at 60 °C for 12 h.

2.5 Synthesis of FePc/C

FePc/C was obtained via a similar method to Ni SA@FePc, except replacing Ni SA/CN with carbon substrate.

2.6 Electrochemical measurements

Biologic VMP3 electrochemical workstation was used in all electrochemical measurements under ambient conditions. The evaluations of electrocatalytic CO_2RR performance were measured in a classical three-electrode H-type cell (separated by Nafion 212 proton exchange membrane) and home-made flow cell (separated by FAA-PK-130 anion exchange membrane) separately. Ag/AgCl electrode was used as a reference electrode. Linear sweep voltammetry (LSV) was measured with a scan rate of 10 $mV{\cdot}s^{-1}$. The electrochemical impedance spectroscopy (EIS) was performed by applying an alternating current (AC) voltage with the amplitude voltage of 10 mV over a frequency range from 100 kHz to 0.1 Hz. The electrochemical active surface area (ECSA) was evaluated by double-layer capacitance (C_{dl}), which was obtained from cyclic voltammetry (CV) results under the potential range of 0.2–0.3 V vs. RHE. The chronoamperometry (CA) tests were conducted at the various potential for 20 min. The gas-phase composition was analyzed on the ThermoFisher Trace 1300 online gas chromatography equipped with PDD and FID detectors. High purity helium (99.9999%) and nitrogen (99.9999%) were employed as a carrier or make-up gas for the chromatography. The liquid products were detected by Bruker AVANCE-III HD 500. All potentials were converted to reversible hydrogen electrodes based on the equation:

$$E_{\mathrm{RHE}} = E_{\mathrm{Ag/AgCl}} + 0.05916 \times \mathrm{pH} + 0.197 \quad (1)$$

The Faradaic efficiency of the gas product was calculated according to the equation:

$$\mathrm{FE} = Q_{\mathrm{CO}}/Q_{\mathrm{total}} = Z \times n \times \mathrm{F}/Q_{\mathrm{total}} \quad (2)$$

Q: the total charge passed through the working electrode. Z: the number of transfer electrons, which is 2 for both CO and H_2. n: the number of moles for a given product. F: Faradaic constant (96,485 $\mathrm{C{\cdot}mol^{-1}}$).

2.7 Computational details

Vienna ab initio Simulation Package (VASP) based on spin-polarized density functional theory was used for all of the computations. The projector-augmented wave (PAW) method and the generalized gradient approximation (GGA) [22, 23] with the Perdew–Burke–Ernzerhof were used to describe the electron-ion interactions. And a plane-wave energy cutoff was set to 400 eV for structure optimization, and the free energies based on the computational hydrogen electrode (CHE) model proposed by Norskov et al. The Brillouin zone was sampled with the single gamma point k-point set and 2 × 2 × 1 k-points [24, 25] for electronic structure. Atomic positions were fully relaxed until the forces were less than 0.03 $\mathrm{eV{\cdot}Å^{-1}}$ and 10^{-5} eV.

The reduction of CO_2 to CO could occur via a pathway by the following steps:

$$CO_2 + (H^+ + e^-) + {*} = {*}COOH$$

$${*}COOH + (H^+ + e^-) = {*}CO + H_2O$$

$${*}CO = {*} + CO$$

3 Results and discussion

3.1 Synthesis and characterization of Ni SA@FePc

The synthesis procedure of Ni SA/CN and Ni SA@FePc is shown in Fig. 1(a). Firstly, 2,2'-bipyridine was coordinated with Ni^{2+} ion to form a homogeneous Ni–N_4 site without agglomeration during the pyrolysis process for Ni SA/CN. Then, Ni SA@FePc was synthesized via a self-assembly method, wherein the heterostructure of Ni SAs and FePc was formed. For comparison, FePc loaded on carbon substrate (FePc/C) was also synthesized by a similar synthetic process. The SEM, TEM, and high-resolution TEM (HR-TEM) images (Figs. S3 and S4 in the Electronic Supplementary Material (ESM)) show Ni SA/CN, FePc/C, and Ni SA@FePc possess interconnected nanosheets morphology without detectable nanoparticles. Ring-like patterns in selected area electron diffraction (SAED) images (Fig. S3 in the ESM) indicate the amorphous states of Ni SA/CN, FePc/C, and Ni SA@FePc, which are well consistent with X-ray diffraction measurements (Fig. S5 in the ESM), excluding the formation of metallic Ni and Fe. Raman and FT-IR spectra confirm the presence of FePC for both FePc/C and Ni SA@FePc (Fig. S6 in the ESM). To verify the dispersion of Ni and Fe species, HAADF-STEM measurement was carried out. As shown in Fig. 1(d), a large number of bright dots (identified as Ni and Fe atoms) are discovered for Ni SA@FePc, indicating well dispersion of single Ni/Fe atoms on CN substrate [26, 27]. Similarly, the atomic-level dispersed Ni or Fe atoms are also observed in Ni SA/CN and FePc/C samples (Figs. S1 and S2 in the ESM), respectively. The corresponding energy-dispersive X-ray spectroscopy (EDS) images (Fig. 1, Figs. S1, and S2 in the ESM) reveal the uniform distribution of Ni, Fe, N, and O elements over Ni SA/CN, FePc/C, and Ni SA@FePc samples. The according Ni loadings are 0.18 at.% and 0.17 at.% for Ni SA/CN and Ni SA@FePc, while Fe loadings are 0.27 at.% and 0.20 at.% for FePc/C and Ni SA@FePc based on inductively coupled plasma optical emission spectrometry detection (Table S2 in the ESM).

To investigate the fine chemical structures of Ni and Fe sites,

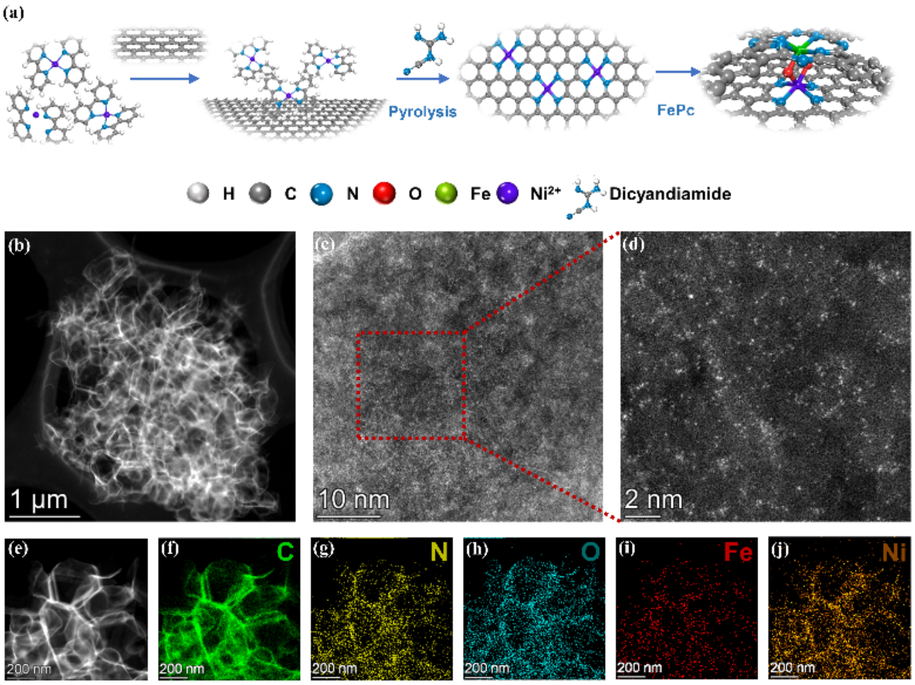

Figure 1 (a) Schematic illustration of the synthesis for Ni SA/CN and Ni SA@FePc. (b)–(d) HAADF-STEM images for Ni SA@FePc. (e)–(i) Corresponding EDS elemental mapping of Ni SA@FePc.

XANES and EXAFS were acquired by synchrotron XAFS techniques (Fig. 2). The XANES profiles of Fe K-edge for FePc/C and Ni SA@FePc exhibit pre-edge peaks at ~ 7,114 eV for FePc and FePc/C (Fig. 2(a)), which can be discovered due to the symmetric Fe–N_4 sites. The near-edges for FePc/C (~ 7,121 eV) and Ni SA@FePc (~ 7,120 eV) are found between these of Fe foil and Fe_2O_3, implying the oxidation states of Fe are between 0 and +3 in both FePc/C and Ni SA@FePc (Fig. 2(b)). Besides, the near-edge of Fe for Ni SA@FePc is located between FePc and FePc/C, in line with the XPS analysis (Fig. S7(a) in the ESM) for Fe $2p_{3/2}$ peaks of Ni SA@FePc (709.4 eV), FePc/C (709.7 eV), and FePc (709.15 eV). The near-edges for Ni SA/CN (~ 8,337 eV) and Ni SA@FePc (~ 8,338 eV) are found between these of Ni foil (8,334 eV) and NiO (8,338 eV) (Fig. 2(d)), implying the oxidation states of Ni are between 0 and +2 in both Ni SA/CN and Ni SA@FePc samples (Fig. 2(e)) [28]. Notably, the near-edge for Ni SA@FePc locates at higher energy compared with Ni SA/CN and thus results in a higher oxidation state of Ni in Ni SA@FePc, which is consistent with the XPS analysis (Fig S7(b) in the ESM). The Ni $2p_{3/2}$ peak of Ni SA@FePc (855.5 eV) appears higher than Ni^0 (852.6 eV) and Ni SA/CN (855.2 eV), further confirming the chemical state of Ni for Ni SA@FePc is higher compared with Ni SA/CN [29]. In addition, both NiPc and Ni SA/CN show pre-edge peaks at ~ 8,334 eV, which can be identified to the planar-shape and highly symmetric Ni–N_x sites [30]. In contrast, Ni SA@FePc exhibits no pre-edge peak at ~ 8,334 eV, revealing the destruction of symmetric Ni–N_x structure. Unexpectedly, Ni SA@FePc shows no pre-edge peak, suggesting that the axial coordination destructs the local square-planar structure [31, 32]. The coordination number (CN) of Fe–N/O, Ni-N/O for Ni SA@FePc is 5.5 and 5.8, respectively (Figs. 2(c), 2(f), and Table S1 in the ESM).

The porous structures of the samples were investigated by nitrogen adsorption and desorption isotherms at 77.3 K (Fig. S11 in the ESM). Ni SA@FePc inherits the porous structure of Ni SA/CN, which is beneficial for mass transportation and exposing abundant active sites for CO_2RR. Besides, Ni SA/CN generates a higher Brunauer–Emmett–Teller (BET) surface area than Ni SA@FePc (Table S3 in the ESM). The slight decrease of BET surface area for Ni SA@FePc could attribute to the introduction of FePc during the self-assembly process in liquid condition, suggesting the homogeneous distribution of FePc on matrix. The pore diameter distribution curves demonstrate the presence of mesopores and micropores with an average size of 3.749 nm for Ni SA@FePc and 3.331 nm for Ni SA/CN (Table S3 in the ESM). Different N species including Ni/Fe–N, pyrrolic N, pyridinic N, graphic N, and quaternary N are presented in the high-resolution N 1s XPS spectra of Ni SA@FePc and Ni SA/CN (Fig. S8(b) in the ESM), and an obvious increase of Ni/Fe–N in SA@FePc compared with Ni SA/CN could ascribe to the Fe–N bonds in FePc, therefore confirming the coordination of Ni/Fe and N atom in Ni SA@FePc and Ni SA/CN samples. In addition, the increased ratio of Fe–O bonds in Ni SA@FePc compared with that in FePc/C and FePc (Fig. S9(b) in the ESM) reveals extra coordination with Fe–N_4 sites in an axial direction in Ni SA@FePc, in line with the fitting results according to FT EXAFS. The CO_2 absorption properties were measured at 273 K by CO_2 absorption and desorption isotherms. As shown in Fig. S12 in the ESM, Ni SA@FePc acquires higher CO_2 absorption capacity (30.41 $cm^3 \cdot g^{-1}$) than that of Ni SA/CN (22.775 $cm^3 \cdot g^{-1}$) and FePc/C (15.437 $cm^3 \cdot g^{-1}$), which can be owing to its more feasible and accessible absorption sites for CO_2 molecules, and thus favorable for boosting the high catalytic performance.

3.2 Electrochemical measurements

The evaluation of electrocatalytic performance for CO_2RR was first implemented in a classical three-electrode H-type cell (Fig. S13 in the ESM) with 0.1 M $KHCO_3$. A significant increase in the current density is observed for Ni SA@FePc when the electrolyte is changed from Ar-saturated to CO_2-saturated electrolyte, disclosing its more favorable CO_2RR process than the competing hydrogen evolution reaction (HER) (Fig. S13(a) in the ESM) [33, 34]. Besides, Ni SA@FePc delivers a larger current density and more positive onset potential compared with Ni SA/CN and FePc/C under CO_2-saturated electrolyte, suggesting the preponderance of Ni SA@FePc for activating CO_2 molecules. Next, CA of CO_2

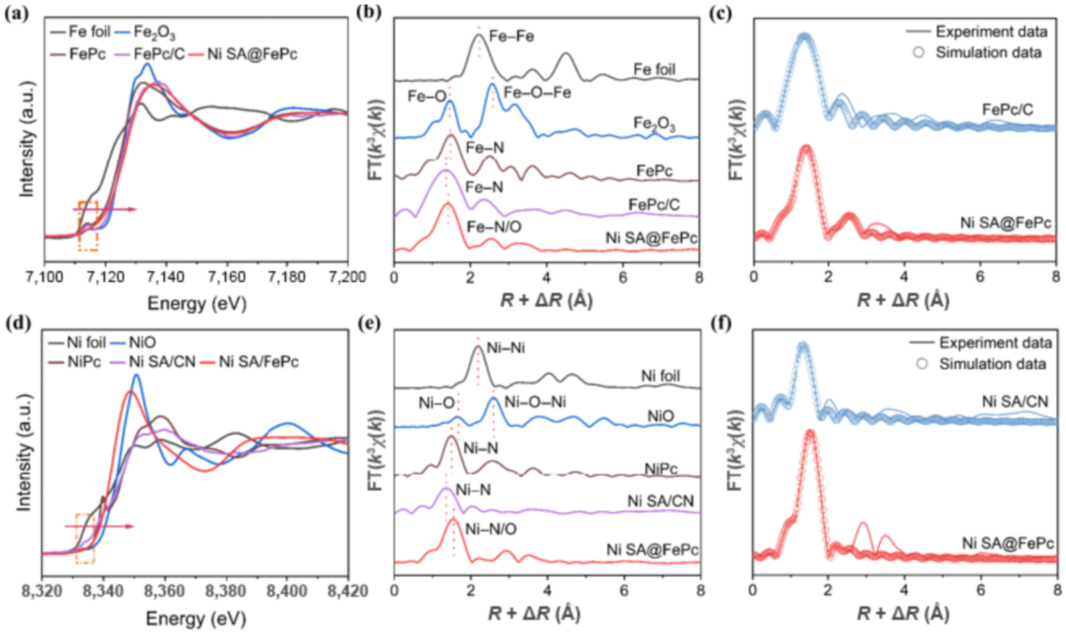

Figure 2 (a) Fe K-edge XANES profiles of Fe foil, Fe_2O_3, FePc, FePc/C, and Ni SA@FePc. (b) Fe K-edge spectra. (c) Fe K-edge FT EXAFS of Ni SA/CN and Ni SA@FePc. (d) Ni K-edge XANES profiles of Ni foil, NiO, NiPc (nickel phthalocyanine), Ni SA/CN, and Ni SA@FePc. (e) Ni K-edge spectra. (f) Ni K-edge FT EXAFS of Ni SA/CN and Ni SA@FePc.

electrolysis was operated over a potential range from −0.2 to −0.8 V vs. RHE without iR compensation, wherein product detection was carried out by online gas chromatography (GC) and offline ^{1}H NMR. As shown in Figs. S15 and S16 in the ESM, only gas products were detected (CO and H_2) in these catalytic systems. Better behavior of Ni SA@FePc in electrocatalysis CO_2RR to CO is achieved regarding its higher FE_{CO} (Fig. S13(c) in the ESM) and larger j_{CO} (Fig. S13(b) in the ESM) than these of Ni SA/CN and FePc/C over the whole applied potentials at −0.5 V vs. RHE. Ni SA@FePc obtains a higher FE_{CO} up to 97.65% than these of Ni SA/CN (95.54%) and FePc/C (95.02%), highlighting its excellent selectivity in electrolysis CO_2 to CO. Moreover, the feasibility of Ni SA@FePc in practical electrocatalytic CO_2 to CO is evaluated in a homemade three-electrode flow cell, with catalyst modified gas diffusion layer (GDL) as work electrode and 0.1 M KOH as an electrolyte, which can greatly alleviate the restriction of CO_2 solubility in a flow cell. Benefitting from this three-phase interface reaction, the CO evolution efficiency is determined by the local catalytic activity of catalysts rather than confined by solubility and diffusion rate. Impressively beneficial from abundant active sites, excellent conductivity, and plentiful pores (Figs. S11 and S12 in the ESM), Ni SA@FePc shows an astonishing CO_2RR performance. As shown in Figs. 3(a)–3(c), Ni SA@FePc displays a large j_{CO} (~ 252 mA·cm^{-2}) and high FE_{CO} up to ~ 99% at an ultralow overpotential (390 mV), which is 2 folder than these for Ni SA/CN (~ 125 mA·cm^{-2}) and 1.4 folder than FePc/C (~ 175 mA·cm^{-2}), demonstrating the superiority of Ni SA@FePc in electrocatalytic CO_2RR [35]. Besides, the Ni SA@FePc maintains above 95% of FE over the whole applied potential range from −0.15 to −0.5 V vs. RHE. Thus, Ni SA is indeed devoted to activating and stabilizing the molecular FePc during the CO_2RR process.

Additionally, a lower Tafel slope (102.7 mV·dec^{-1}, Fig. 3(d)) is obtained by Ni SA@FePc in electrocatalysis CO_2 to CO compared with Ni SA/CN (121.9 mV·dec^{-1}), FePc/C (118.8 mV·dec^{-1}), and FePc (180.37 mV·dec^{-1}), indicating its faster reaction kinetics and the first electron transfer step for the generation of *COOH species as the rate-determining step (RDS) [36]. It is thus clear that Ni SA substrate plays an important role in enhancing the CO_2RR catalytic performance of FePc.

Interestingly, bare FePc exhibits negligible CO current density (~ 1 mA·cm^{-2}) at the whole applied potentials and inferior faradaic efficiency (below 36%), which is consistent with the results using H-type cell (j_{CO}, ~ 0.2 mA·cm^{-2} and FE_{CO}, 28.8%). The negligible j_{CO} and extremely low FE_{CO} are gained for bare FePc in both H-type cell and flow cell due to its low conductivity, which is confirmed by the EIS analysis (Fig. 3(f)). When supported on a carbon substrate, FePc/C shows obvious improvement in conductivity and thus higher j_{CO} and FE_{CO}. However, the j_{CO} and FE_{CO} of FePc decay significantly at high potentials (from −0.5 V vs. RHE, Figs. S13 (b) and S13(c) in the ESM), indicating the instability of FePc during the CO_2 electrolysis process [37, 38]. In sharp contrast, j_{CO} and FE_{CO} of Ni SA@FePc maintain even at high potentials. Therefore, despite activating the FePc in accelerating electrocatalysis CO_2RR, Ni SA substrate also contributes to stabilizing the molecular catalytic centers of Ni SA@FePc.

The electrochemical capacitance measurements were also implemented to evaluate the ECSA by acquiring the C_{dl} as

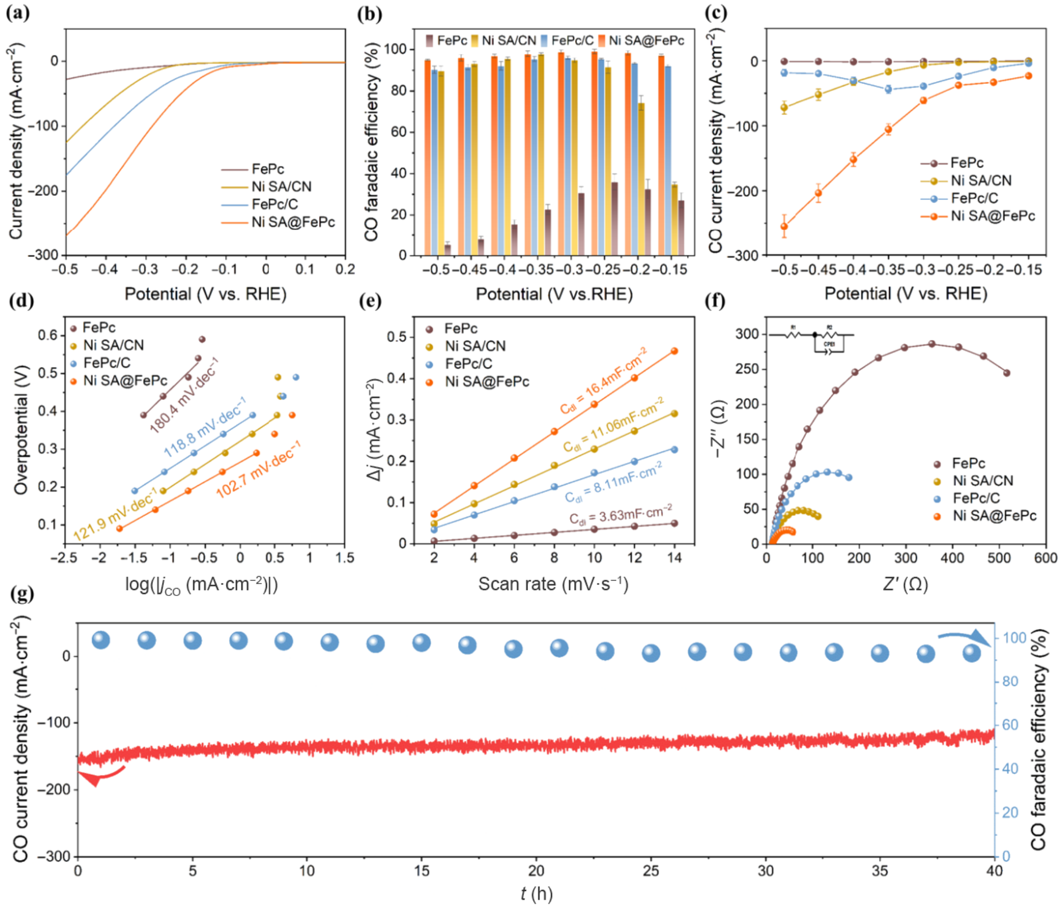

Figure 3 (a) Linear sweep voltammetry curves of FePc, Ni SA/CN, FePc/C, and Ni SA@FePc under CO_2 gas flow in 0.1 M KOH electrolyte with home-made flow cell. (b) CO Faradaic efficiency for FePc, Ni SA/CN, FePc/C, and Ni SA@FePc. (c) CO current density for FePc, Ni SA/CN, FePc/C, and Ni SA@FePc. (d) Tafel slpoes of FePc, Ni SA/CN, FePc/C, and Ni SA@FePc. (e) Double layer capacity and (f) Nyquist plots for FePc, Ni SA/CN, FePc/C, and Ni SA@FePc. (g) Long-term electrolysis of Ni SA@FePc at −0.4 V vs. RHE.

reference (Fig. 3(e) and Fig. S20 in the ESM). Ni SA@FePc shows a much higher normalized C_{dl} of 16.4 mF·cm^{-2} than these of FePc (3.63 mF·cm^{-2}), Ni SA/CN (11.06 mF·cm^{-2}), and FePc/C (8.11 mF·cm^{-2}) that Ni SA@FePc possesses significant larger ECSA, which is favorable for exposing more electrochemical active sites [39]. Besides, Ni SA@FePc also shows elevated electron transfer kinetic during the CO_2RR process compared with Ni SA/CN and FePc/C as it demonstrates lower charge transfer resistance based on the Nyquist plots (Fig. 3(f)), illustrating the more facilitated pathway to conduct charges for enhancing CO_2 adsorption and activation to achieve the purpose of CO evolution on Ni SA@FePc. Thereby, Ni SA@FePc with a high density of active sites, large specific surface area, and high conductivity has incomparable superiority in electrocatalytic CO_2 to CO compared with Ni SA/CN and FePc/C.

The long-term stability in the flow cell was examined at –0.4 V vs. RHE in 0.1 M KOH electrolyte. As shown in Fig. 3(g), only slight attenuation of j_{CO} (~ 150 mA·cm^{-2}) with FE_{CO} above 90% under 20 h uninterrupted electrolysis is observed for Ni SA@FePc, elucidating the preeminent stability and superior selectivity of catalytic sites for CO_2 reduction under large current density condition. Besides, long-time durability of Ni SA@FePc (Fig. S13(d) in the ESM) in an H-type cell is also tested, and no apparent degradation of current density (~ 18 mA·cm^{-2}) under 20 h continuous electrocatalysis at –0.7 V vs. RHE. The slight decay of CO faradaic efficiency (~ 97% to 91%) likely originates from the carbonate accumulation on the surface of the electrode, which could cover up the active sites. The ex-situ XRD (Fig. S17 in the ESM), UV-vis spectra (Fig. S18 in the ESM), and XPS analysis (Fig. S19 in the ESM) exclude the generation of metallic Ni/Fe phases in Ni SA@FePc sample after 20 h electrolysis. It is thus concluded that the stable molecular heterogeneous structure of Ni SA@FePc with inherited advantages of single Ni atom sites and molecular FePc, as well as new regulated catalytic centers, demonstrating excellent feasibility in electrocatalysis CO_2RR to CO.

3.3 DFT calculations

To understand the underlying catalytic mechanism for CO_2 activation and reduction, DFT calculations were performed to construct appropriate models in line with XAFS results and illustrate the real active sites on theoretical sights [40]. According to the fitting data of EXAFS, the ideal models of Ni SA@FePc were built with NiN_4-O_2-FePc three-dimensional structure shown in Fig. S23 in the ESM, denoted as model 1 named NiN_4-O_2-FePc-1 (Fig. S23(b) in the ESM), model 2 named NiN_4-O_2-FePc-2 (Fig. S23(c) in the ESM), and model 3 named NiN_4-O_2-FePc-3 (Fig. S23(d) in the ESM), respectively, in which a concave Fe–N_4 center was formed due to the axial stretching by oxygen atoms. Meanwhile, a raised Ni–N_4 (defined as model 5 named NiN_4) coordination environment was also appeared by interacting with oxygen atoms. The introduction of oxygen atoms bridge Ni and Fe species and break the in-plane metal–N_4 centers, confirmed by XANES profiles. Besides, the model of Ni SA/CN (Fig. 4(b) and Fig. S21(a) in the ESM) was established with Ni–N_4 coordination structures embedded in graphene and FePc/C (defined as model 4 named FePc/C as shown in Fig. 4(c) and Fig. S22(a) in the ESM) was considered as a graphene-FePc double-layer structure, interacting with Van der Waals force. Herein we put forward three models of Ni SA@FePc to verify the reaction site for CO_2RR (Fig. 4) because of the novel concave structure. As shown in Fig 4(a), model 2 (NiN_4-O_2-FePc-2, Fig. 4(e) and Fig. S23(c) in the ESM) exhibits lowest energy barrier for the adsorption of *COOH (0.01 eV) compared with model 1 (NiN_4-O_2-FePc-1, 2.06 eV, Fig. 4(d) and Fig. S23(b) in the ESM), model 3 (NiN_4-O_2-FePc-3, 0.97 eV, Fig. 4(f) and Fig. S23(d) in the ESM), model 4 (FePc/C, 1.41 eV, Fig. S22(a) in the ESM), and model 5 (NiN_4, 1.85 eV, Fig. S21(a) in the ESM).

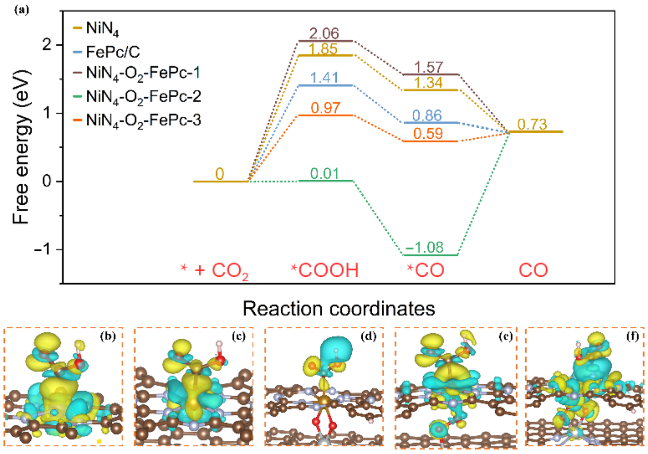

Figure 4 (a) The Gibbs free energy plots of CO_2RR on different models. Inset: adsorption configurations of *COOH on a different surface. (b)–(f) Corresponding charge density difference plots for different models.

Charge density difference plots (Figs. 4(b)–4(f)) illustrate that, upon the adsorption of *COOH, model 1 shows that there is less electronic interaction between COOH and Fe, suggesting that weakest adsorption for *COOH. In contrast, the adsorption center of model 2 is pentacoordinate Fe site, where electrons could be provided to *COOH and strengthen the interaction between *COOH and Fe site, resulting in difficult desorption of CO [41]. Differently, model 3 manifests a moderate energy barrier for *COOH adsorption and spontaneous desorption for *CO, indicating an RDS of *COOH adsorption, consistent with the results based on Tafel slopes analysis. The Fe site with hex coordinate environment owns inferior charge distribution and adsorption of *COOH, illustrating its inapplicability as an active site. Besides, the strong interaction of Fe and O atoms result in the reconstruction of FePc and the stretch of Fe–N bonds, which motivates the catalytic activity and increases the charge distribution. Importantly, such transformation promotes the adsorption for *COOH on N atoms next to Fe atoms. It also enables a spontaneous step for *CO desorption and the obviously improved catalytic performance along with activating more N active sites by sacrificing Fe sites, accounting for the high CO_2RR performance in a flow cell on Ni SA@FePc (Fig. 3).

4 Conclusion

In summary, we have developed a single atom Ni regulated FePc molecular catalyst (Ni SA@FePc) and achieved a great enhancement in electrocatalytic CO_2RR along with a satisfying CO selectivity with more than 90% CO Faradaic efficiency in a wide potential window (from –0.2 V to –0.8 V vs. RHE), high current density (~ 252 mA·cm^{-2}) at a low overpotential (390 mV) and long-term stability (20 h) in alkaline electrolyte. Combining XAFS techniques and DFT calculations, we propose an original concave Fe–N_4 and raised Ni–N_4 three-dimension heterogeneous structure for Ni SA@FePc, which are bridged by two O atoms. Besides, the interaction between Ni and Fe species further stabilizes the unstable FePc molecules and provides new active sites (the N atom next to Fe atom) for CO_2RR, in line with the evaluation of CO_2RR, respectively. This regulation strategy illustrates a prospective avenue in pursuing atomic-level motifs for highly efficient electrocatalysis by regulating the coordination of the catalytic centers and speeding up the fundamental studies in catalytic mechanisms.

Acknowledgments

H. X. Z. acknowledges funding from the Alexander von Humboldt Foundation. This work was supported by the National Natural Science Foundation of China (No. 21725103), National Key R&D Program of China (No. 2019YFA0705704), the Strategic Priority Research Program of the Chinese Academy of Sciences (No. XDA21010210), Jilin Province Science and Technology Development Plan Funding Project (No. 20200201079JC), Changchun Science and Technology Development Plan Funding Project (No. 19SS010), Jilin Province Capital Construction Funds Project (No. 2020C026-1), and the K. C. Wong Education Foundation (No. GJTD-2018-09).

Electronic Supplementary Material: Supplementary material (TEM, HR-TEM, HAADF-STEM, XRD, FT-IR, Raman, XPS, ^{1}H-NMR, UV–Vis, electrochemical capacitance, and DFT models) is available in the online version of this article at https://dx.doi.org/10.1007/s12274-022-4197-6.

References

[1] Chu, S.; Cui, Y.; Liu, N. The path towards sustainable energy. *Nat. Mater.* **2017**, *16*, 16–22.

[2] Mitchell, S.; Pérez-Ramírez, J. Single atom catalysis: A decade of stunning progress and the promise for a bright future. *Nat. Commun.* **2020**, *11*, 4302.

[3] Obama, B. The irreversible momentum of clean energy. *Science* **2017**, *355*, 126–129.

[4] Gu, J.; Hsu, C. S.; Bai, L. C.; Chen, H. M.; Hu, X. L. Atomically dispersed Fe^{3+} sites catalyze efficient CO_2 electroreduction to CO. *Science* **2019**, *364*, 1091–1094.

[5] Zheng, T. T.; Jiang, K.; Ta, N.; Hu, Y. F.; Zeng, J.; Liu, J. Y.; Wang, H. T. Large-scale and highly selective CO_2 electrocatalytic reduction on nickel single-atom catalyst. *Joule* **2019**, *3*, 265–278.

[6] Wu, Y. S.; Jiang, Z.; Lu, X.; Liang, Y. Y.; Wang, H. L. Domino electroreduction of CO_2 to methanol on a molecular catalyst. *Nature* **2019**, *575*, 639–642.

[7] Wang, Y. C.; Xu, L.; Zhan, L. S.; Yang, P. Y.; Tang, S. H.; Liu, M. J.; Zhao, X.; Xiong, Y.; Chen, Z. Y.; Lei, Y. H. Electron accumulation enables Bi efficient CO_2 reduction for formate production to boost clean Zn-CO_2 batteries. *Nano Energy* **2022**, *92*, 106780.

[8] Zhang, X.; Wu, Z. S.; Zhang, X.; Li, L. W.; Li, Y. Y.; Xu, H. M.; Li, X. X.; Yu, X. L.; Zhang, Z. S.; Liang, Y. Y. et al. Highly selective and active CO_2 reduction electrocatalysts based on cobalt phthalocyanine/carbon nanotube hybrid structures. *Nat. Commun.* **2017**, *8*, 14675.

[9] Zhong, M.; Tran, K.; Min, Y. M.; Wang, C. H.; Wang, Z. Y.; Dinh, C. T.; De Luna, P.; Yu, Z. Q.; Rasouli, A. S.; Brodersen, P. et al. Accelerated discovery of CO_2 electrocatalysts using active machine learning. *Nature* **2020**, *581*, 178–183.

[10] Ju, W.; Bagger, A.; Hao, G. P.; Varela, A. S.; Sinev, I.; Bon, V.; Roldan Cuenya, B.; Kaskel, S.; Rossmeisl, J.; Strasser, P. Understanding activity and selectivity of metal-nitrogen-doped carbon catalysts for electrochemical reduction of CO_2. *Nat. Commun.* **2017**, *8*, 944.

[11] Zhang, T. Y.; Han, X.; Yang, H. B.; Han, A. J.; Hu, E. Y.; Li, Y. P.; Yang, X. Q.; Wang, L.; Liu, J. F.; Liu, B. Atomically dispersed nickel(I) on an alloy-encapsulated nitrogen-doped carbon nanotube array for high-performance electrochemical CO_2 reduction reaction. *Angew. Chem., Int. Ed.* **2020**, *59*, 12055–12061.

[12] Chen, K. J.; Liu, K.; An, P. D.; Li, H. J. W.; Lin, Y. Y.; Hu, J. H.; Jia, C. K.; Fu, J. W.; Li, H. M.; Liu, H. et al. Iron phthalocyanine with coordination induced electronic localization to boost oxygen reduction reaction. *Nat. Commun.* **2020**, *11*, 4173.

[13] Zhang, X.; Wang, Y.; Gu, M.; Wang, M. Y.; Zhang, Z. S.; Pan, W. Y.; Jiang, Z.; Zheng, H. Z.; Lucero, M.; Wang, H. L. et al. Molecular engineering of dispersed nickel phthalocyanines on carbon nanotubes for selective CO_2 reduction. *Nat. Energy* **2020**, *5*, 684–692.

[14] Hou, Y.; Qiu, M.; Kim, M. G.; Liu, P.; Nam, G.; Zhang, T.; Zhuang, X. D.; Yang, B.; Cho, J.; Chen, M. W. et al. Atomically dispersed nickel-nitrogen-sulfur species anchored on porous carbon nanosheets for efficient water oxidation. *Nat. Commun.* **2019**, *10*, 1392.

[15] Sun, X. H.; Tuo, Y. X.; Ye, C. L.; Chen, C.; Lu, Q.; Li, G. N.; Jiang, P.; Chen, S. H.; Zhu, P.; Ma, M. et al. Phosphorus induced electron localization of single iron sites for boosted CO_2 electroreduction reaction. *Angew. Chem., Int. Ed.* **2021**, *60*, 23614–23618.

[16] Yang, H. B.; Hung, S. F.; Liu, S.; Yuan, K. D.; Miao, S.; Zhang, L. P.; Huang, X.; Wang, H. Y.; Cai, W. Z.; Chen, R. et al. Atomically dispersed Ni(I) as the active site for electrochemical CO_2 reduction. *Nat. Energy* **2018**, *3*, 140–147.

[17] Jiang, K.; Siahrostami, S.; Zheng, T. T.; Hu, Y. F.; Hwang, S.; Stavitski, E.; Peng, Y. D.; Dynes, J.; Gangisetty, M.; Su, D. et al. Isolated Ni single atoms in graphene nanosheets for high-performance CO_2 reduction. *Energy Environ. Sci.* **2018**, *11*, 893–903.

[18] Jiang, Z. L.; Wang, T.; Pei, J. J.; Shang, H. S.; Zhou, D. N.; Li, H. J.; Dong, J. C.; Wang, Y.; Cao, R.; Zhuang, Z. B. et al. Discovery of main group single Sb–N_4 active sites for CO_2 electroreduction to formate with high efficiency. *Energy Environ. Sci.* **2020**, *13*, 2856–2863.

[19] Lin, L.; Li, H. B.; Yan, C. C.; Li, H. F.; Si, R.; Li, M. R.; Xiao, J. P.; Wang, G. X.; Bao, X. H. Synergistic catalysis over iron-nitrogen sites anchored with cobalt phthalocyanine for efficient CO_2 electroreduction. *Adv. Mater.* **2019**, *31*, 1903470.

[20] Ren, S. X.; Joulié, D.; Salvatore, D.; Torbensen, K.; Wang, M.; Robert, M.; Berlinguette, C. P. Molecular electrocatalysts can mediate fast, selective CO_2 reduction in a flow cell. *Science* **2019**, *365*, 367–369.

[21] Ren, W. H.; Tan, X.; Yang, W. F.; Jia, C.; Xu, S. M.; Wang, K. X.; Smith, S. C.; Zhao, C. Isolated diatomic Ni-Fe metal-nitrogen sites for synergistic electroreduction of CO_2. *Angew. Chem., Int. Ed.* **2019**, *58*, 6972–6976.

[22] Blöchl, P. E. Projector augmented-wave method. *Phys. Rev. B* **1994**, *50*, 17953–17979.

[23] Perdew, J. P.; Burke, K.; Ernzerhof, M. Generalized gradient approximation made simple. *Phys. Rev. Lett.* **1996**, *77*, 3865–3868.

[24] Wang, V.; Xu, N.; Liu, J. C.; Tang, G.; Geng, W. T. VASPKIT: A user-friendly interface facilitating high-throughput computing and analysis using VASP code. *Comput. Phys. Commun.* **2021**, *267*, 108033.

[25] Jing, H. Y.; Zhu, P.; Zheng, X. B.; Zhang, Z. D.; Wang, D. S.; Li, Y. D. Theory-oriented screening and discovery of advanced energy transformation materials in electrocatalysis. *Adv. Powder Mater.* **2021**, 100013.

[26] Zhou, H.; Yang, T.; Kou, Z. K.; Shen, L.; Zhao, Y. F.; Wang, Z. Y.; Wang, X. Q.; Yang, Z. K.; Du, J. Y.; Xu, J. et al. Negative pressure pyrolysis induced highly accessible single sites dispersed on 3D graphene frameworks for enhanced oxygen reduction. *Angew. Chem., Int. Ed.* **2020**, *59*, 20465–20469.

[27] Zhu, Z. J.; Yin, H. J.; Wang, Y.; Chuang, C. H.; Xing, L.; Dong, M. Y.; Lu, Y. R.; Casillas-Garcia, G.; Zheng, Y. L.; Chen, S. et al. Coexisting single-atomic Fe and Ni sites on hierarchically ordered porous carbon as a highly efficient ORR electrocatalyst. *Adv. Mater.* **2020**, *32*, 2004670.

[28] Yang, H. P.; Lin, Q.; Zhang, C.; Yu, X. Y.; Cheng, Z.; Li, G. D.; Hu, Q.; Ren, X. Z.; Zhang, Q. L.; Liu, J. H. et al. Carbon dioxide electroreduction on single-atom nickel decorated carbon membranes with industry compatible current densities. *Nat. Commun.* **2020**, *11*, 593.

[29] Chen, Y. J.; Gao, R.; Ji, S. F.; Li, H. J.; Tang, K.; Jiang, P.; Hu, H. B.; Zhang, Z. D.; Hao, H. G.; Qu, Q. Y. et al. Atomic-level modulation of electronic density at cobalt single-atom sites derived

from metal–organic frameworks: Enhanced oxygen reduction performance. *Angew. Chem., Int. Ed.* **2021**, *60*, 3212–3221.

[30] Yang, Q. H.; Yang, C. C.; Lin, C. H.; Jiang, H. L. Metal–organic framework-derived hollow N-doped porous carbon with ultrahigh concentrations of single Zn atoms for efficient carbon dioxide conversion. *Angew. Chem., Int. Ed.* **2019**, *58*, 3511–3515.

[31] Zhang, B. X.; Zhang, J. L.; Shi, J. B.; Tan, D. X.; Liu, L. F.; Zhang, F. Y.; Lu, C.; Su, Z. Z.; Tan, X. N.; Cheng, X. Y. et al. Manganese acting as a high-performance heterogeneous electrocatalyst in carbon dioxide reduction. *Nat. Commun.* **2019**, *10*, 2980.

[32] Luo, F.; Roy, A.; Silvioli, L.; Cullen, D. A.; Zitolo, A.; Sougrati, M. T.; Oguz, I. C.; Mineva, T.; Teschner, D.; Wagner, S. et al. P-block single-metal-site tin/nitrogen-doped carbon fuel cell cathode catalyst for oxygen reduction reaction. *Nat. Mater.* **2020**, *19*, 1215–1223.

[33] Zang, W. J.; Sun, T.; Yang, T.; Xi, S. B.; Waqar, M.; Kou, Z. K.; Lyu, Z.; Feng, Y. P.; Wang, J.; Pennycook, S. J. Efficient hydrogen evolution of oxidized Ni–N_3 defective sites for alkaline freshwater and seawater electrolysis. *Adv. Mater.* **2021**, *33*, 2003846.

[34] Yan, C. C.; Li, H. B.; Ye, Y. F.; Wu, H. H.; Cai, F.; Si, R.; Xiao, J. P.; Miao, S.; Xie, S. H.; Yang, F. et al. Coordinatively unsaturated nickel-nitrogen sites towards selective and high-rate CO_2 electroreduction. *Energy Environ. Sci.* **2018**, *11*, 1204–1210.

[35] Voiry, D.; Shin, H. S.; Loh, K. P.; Chhowalla, M. Low-dimensional catalysts for hydrogen evolution and CO_2 reduction. *Nat. Rev. Chem.* **2018**, *2*, 0105.

[36] Kong, X. D.; Ke, J. W.; Wang, Z. Q.; Liu, Y.; Wang, Y. B.; Zhou, W. R.; Yang, Z. W.; Yan, W. S.; Geng, Z. G.; Zeng, J. Co-based molecular catalysts for efficient CO_2 reduction via regulating spin states. *Appl. Catal. B:Environ.* **2021**, *290*, 120067.

[37] Liu, X.; Jiao, Y.; Zheng, Y.; Jaroniec, M.; Qiao, S. Z. Building up a picture of the electrocatalytic nitrogen reduction activity of transition metal single-atom catalysts. *J. Am. Chem. Soc.* **2019**, *141*, 9664–9672.

[38] Bénisvy, L.; Halut, S.; Donnadieu, B.; Tuchagues, J. P.; Chottard, J. C.; Li, Y. Monomeric iron(II) hydroxo and iron(III) dihydroxo complexes stabilized by intermolecular hydrogen bonding. *Inorg. Chem.* **2006**, *45*, 2403–2405.

[39] Hikichi, S.; Ogihara, T.; Fujisawa, K.; Kitajima, N.; Akita, M.; Moro-Oka, Y. Synthesis and characterization of the benzoylformato ferrous complexes with the hindered tris(pyrazolyl)borate ligand as a structural model for mononuclear non-heme iron enzymes. *Inorg. Chem.* **1997**, *36*, 4539–4547.

[40] Chen, S. H.; Li, W. H.; Jiang, W. J.; Yang, J. R.; Zhu, J. X.; Wang, L. Q.; Ou, H. H.; Zhuang, Z. C.; Chen, M. Z.; Sun, X. H. et al. MOF encapsulating N-heterocyclic carbene-ligated copper single-atom site catalyst towards efficient methane electrosynthesis. *Angew. Chem., Int. Ed.* **2022**, *61*, e202114450.

[41] Wang, Y. N.; Zheng, Y.; Han, C.; Chen, W. Surface charge transfer doping for two-dimensional semiconductor-based electronic and optoelectronic devices. *Nano Res.* **2021**, *14*, 1682–1697.